Research Square

Preprints are preliminary reports that have not undergone peer review.
They should not be considered conclusive, used to inform clinical practice,
or referenced by the media as validated information.

Friction Modeling in Revolute and Spherical Joints for Constrained Multibody Systems

Marco Morandini
Politecnico di Milano
Pierangelo Masarati
pierangelo.masarati@polimi.it
Politecnico di Milano

Research Article

Keywords: Revolute Joint, Spherical Joint, Friction, Coulomb Friction, Modified LuGre Friction

Posted Date: November 20th, 2026

DOI: https://doi.org/10.21203/rs.3.rs-11142778/v1

License: This work is licensed under a Creative Commons Attribution 4.0 International License.
Read Full License

Additional Declarations: Competing interest reported. The second author, Pierangelo Masarati, is an Associate Editor of Multibody System Dynamics, but was not involved in the peer review process at any stage. All other authors have no competing interests to declare that are relevant to the content of this article.

Friction Modeling in Revolute and Spherical Joints for Constrained Multibody Systems

Marco Morandini[1] and Pierangelo Masarati[1*]

[1*]Department of Aerospace Science and Technology, Politecnico di Milano, via La Masa 34, Milan, 20156, Italy.

*Corresponding author(s). E-mail(s): pierangelo.masarati@polimi.it;
Contributing authors: marco.morandini@polimi.it;

Abstract

This work presents a formulation for modeling friction in revolute and spherical joints within a general-purpose multibody framework. The approach extends friction models commonly used for planar contacts to joints with three-dimensional relative rotation while preserving numerical robustness and computational efficiency. Both a classical Coulomb model and a dynamic LuGre formulation are considered, allowing the representation of stick-slip transitions, pre-sliding effects, and velocity-dependent friction behavior.

Unlike previous approaches, including some commercial implementations, the proposed formulation treats the joint reaction as the normal contact force rather than the total reaction force. Friction forces and moments are then expressed directly as functions of the friction coefficients and the normal reaction force, yielding a simpler and more modular formulation in which different friction laws can be incorporated without modifying the underlying multibody equations.

The methodology is assessed using benchmark problems and applied to a generic tiltrotor gimbal assembly representative of the motivating application characterized by multiple interacting revolute and frictional joints and redundant constraints. The results show that joint friction can significantly affect the dynamic response and energy dissipation of the system, while the proposed formulation remains effective in the presence of sticking conditions and complex joint interactions. The approach provides an efficient framework for the simulation of articulated mechanical and aerospace systems with frictional revolute and spherical joints.

Keywords: Revolute Joint, Spherical Joint, Friction, Coulomb Friction, Modified LuGre Friction

1 Introduction

Friction is often regarded as a secondary modeling aspect in multibody simulations, especially when the focus is on system-level dynamics, structural flexibility, or control interactions. However, joint friction can significantly influence system dynamics, stability, energy dissipation, and transient response. This is particularly relevant in articulated mechanical systems, especially those used in aerospace applications, where relatively small friction torques may often alter load transmission paths, affect modal damping, or trigger nonlinear phenomena [1–6]. Recent studies have addressed both the modeling and identification of joint friction in multibody systems, including physics-based and data-driven approaches [7–9]. More generally, comprehensive reviews of friction models emphasize the complexity of frictional behavior and the dependence of appropriate model choice on the phenomena to be represented [10].

Among the various types of joints used in aerospace and mechanical systems, revolute and spherical joints are notable for providing large rotational freedom while transmitting significant loads. Examples include articulated hub mechanisms in rotorcraft, gimbal assemblies, actuation systems, suspension components, and robotic joints. Flexible-joint robotic systems, in particular, have motivated extensive studies of nonlinear joint phenomena, including friction and other effects that can influence their dynamic behavior [11]. Contact and joint mechanics have also been extensively investigated in the context of multibody dynamics, including both regularized and nonsmooth formulations [12]. In particular, spherical clearance joints have been shown to affect the predicted kinematics, dynamics, and reaction loads of spatial multibody systems [13]. While spherical joints and their contact behavior have therefore received considerable attention, formulations specifically addressing friction in continuously constrained spherical joints remain comparatively limited.

Many multibody formulations either neglect friction entirely or rely on simplified viscous approximations of sliding friction that are unable to reproduce relevant nonlinear effects such as stiction (static friction that must be overcome to initiate motion), pre-sliding displacement, or velocity-dependent transitions.

Several friction models have been proposed for translational and planar contacts, ranging from classical Coulomb friction laws to more sophisticated dynamic models such as the LuGre formulation [14]. The importance of accounting for such phenomena in multibody simulations has been demonstrated in studies addressing joint friction, stick-slip behavior, and friction in flexible multibody systems [8, 9]. Reviews specifically addressing friction modeling in multibody dynamics have also been presented by Pennestrì et al. [15] and Marques et al. [4]. Dynamic friction models are attractive because they provide a continuous representation of the transition between sticking and sliding regimes while capturing effects such as hysteresis (history-dependent behavior) and rate dependence (variation with velocity) [16]. However, extending these models to fully three-dimensional rotational motion is not straightforward, particularly within constrained multibody formulations, where robustness and numerical efficiency are essential.

The present work, derived from [17], addresses this issue by introducing friction models for revolute and spherical joints within a general-purpose multibody framework. The reference implementation is within the free, general-purpose multibody

solver MBDyn[1] [18]. The formulation of friction is developed consistently with the treatment of kinematic constraints and generalized forces of the multibody framework, enabling the direct inclusion of friction torques arising from the relative angular motion between connected bodies. Both a Coulomb-type formulation (representing a computationally inexpensive static description) and a LuGre-inspired dynamic model (providing a more physically representative dynamic approach) are considered, enabling direct comparison between these modeling strategies.

The proposed methodology is assessed using progressively more representative examples, culminating in the analysis of a representative tiltrotor gimbal assembly motivated by ongoing investigations on whirl-flutter phenomena in tiltrotor wind-tunnel models, where friction within multiple revolute and spherical joints may contribute significantly to the observed dynamical behavior, requiring a physically meaningful yet numerically robust treatment.

A first key aspect of this paper is the reformulation of revolute- and spherical-joint reactions, in which the constraint reactions represent the normal contact forces and the friction coefficients become algebraic unknowns. Thus, friction contributes not only a moment, but also a force component. This approach differs from those adopted by many commercial multibody solvers, where friction is represented solely by a friction-induced moment. This moment is typically calculated from the friction coefficient and the total resultant force, an approximation that may overestimate friction but substantially simplifies the joint formulation. For example, in revolute joints[2] in ANSYS Mechanical Application, the tangential frictional stress is assumed to be uniformly distributed around the joint. Consequently, the friction forces cancel, leaving only a net friction torque; the friction force itself is neither calculated nor reported. In ADAMS,[3] only the reaction moment is considered, while the reaction force is neglected. In COMSOL,[4] joints are treated as abstractions, so the normal reaction force on which the friction force should depend is not uniquely defined. Several methods are therefore available for estimating the normal force associated with a given joint, and the user must choose the most suitable one.

The spherical joint formulation requires the definition of a local reference system at the point of contact in order to track the state of the friction coefficient along two independent directions; this is addressed, avoiding possible parametrization singularities, by integrating its evolution throughout the simulation. Both the revolute and spherical joints intentionally assume, as explained in Sect. 2, the joint to be lightly loaded, with a localized contact region. Both Coulomb and LuGre friction models are considered, with the implementation clearly separating the joint formulation from the friction model, which can therefore be changed transparently. The paper is organized as follows. After introducing the governing friction formulations and their implementation within the multibody equations, the benchmark examples are presented and

[1] https://www.mbdyn.org/, last accessed September 2026.
[2] https://ansyshelp.ansys.com/public/account/secured?returnurl=////Views/Secured/corp/v242/en/wb_sim/ds_joint_friction_joint_types.html, last accessed September 2026.
[3] https://nexus.hexagon.com/documentationcenter/en-US/bundle/simd_2023.1_r2022/page/simd_2023.1_r2022/simd4catia_motion_guide/ref_motion_guidev2/TOC.Friction.Results.xhtml, last accessed September 2026.
[4] https://doc.comsol.com/6.4/docserver/#!/com.comsol.help.mbd/mbd_ug_theory.4.21.html, last accessed September 2026.

discussed, followed by the application to the representative gimbal assembly and a discussion of the implications of friction modeling for complex articulated aerospace systems.

2 Formulation

Multibody problems are commonly formulated using either minimal-coordinate or redundant-coordinate approaches, which differ in the treatment of kinematic constraints. In the former approach, constraints are embedded in the kinematic description and only independent degrees of freedom are retained [19]. In the latter, the equations of motion are augmented by algebraic constraint equations and the associated reaction forces, represented by Lagrange multipliers [20]. A key advantage of the latter approach is that constraint reactions become explicit unknowns, which simplifies the formulation of friction forces that depend on them.

In this work, a redundant-coordinate formulation is adopted. The equations of motion of the unconstrained system take the form

$$\mathbf{M}(\mathbf{x})\ddot{\mathbf{x}} = \mathbf{w}(\mathbf{x}, \dot{\mathbf{x}}, t), \tag{1}$$

with the mass matrix $\mathbf{M}$, the coordinates $\mathbf{x}$, and the external forces $\mathbf{w}$, are complemented by a set of kinematic constraint equations (without loss of generality in holonomic—actually, scleronomic—form)

$$\boldsymbol{\phi}(\mathbf{x}) = \mathbf{0} \tag{2}$$

(dependence on coordinates and time is omitted hereafter for brevity). which introduce constraint reactions in the equations of motion, Eq. (1), namely

$$\mathbf{M}\ddot{\mathbf{x}} + \boldsymbol{\phi}_{/\mathbf{x}}^T \boldsymbol{\lambda} = \mathbf{w}, \tag{3}$$

where $\boldsymbol{\phi}_{/\mathbf{x}}$ is the constraint Jacobian matrix and $\boldsymbol{\lambda}$ are the corresponding Lagrange multipliers, together forming the constraint reaction forces $\mathbf{w}_c = -\boldsymbol{\phi}_{/\mathbf{x}}^T \boldsymbol{\lambda}$. The problem resulting from the union of Eqs. (3) and (2) is a system of differential-algebraic equations (DAE) of index 3.

An ideal revolute joint constrains five components of relative motion between two nodes, indicated as a and b: three components of displacement and two components of rotation. Only relative rotation about a prescribed axis is allowed. An ideal spherical joint only constrains the three components of relative displacement. The latter can be formulated by enforcing coincidence of the joint centers, namely

$$\boldsymbol{\phi} = (\mathbf{x}_a + \mathbf{R}_a \mathbf{d}_a) - (\mathbf{x}_b + \mathbf{R}_b \mathbf{d}_b) = \mathbf{0}, \tag{4}$$

where $\mathbf{x}_i$ is the position of node i ($i = a, b$), $\mathbf{R}_i$ is its orientation, and $\mathbf{d}_i$ is the position of the spherical joint's center in node i's reference frame.

The revolute joint of Fig. 1 adds two constraint equations to Eq. (4); without loss of generality, they constrain relative rotation about local axes 1 and 2; namely, the

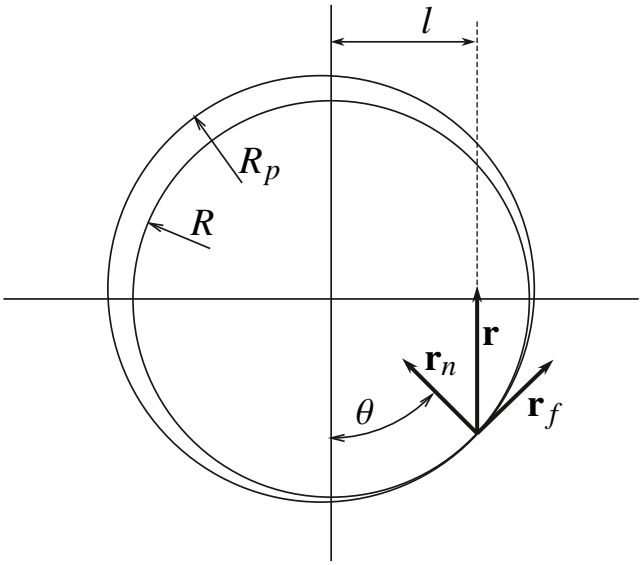

Fig. 1: Revolute joint.

joint's axis is local axis 3. According to Fig. 1, a revolute joint of radius R exchanges a reaction force $\mathbf{r}$ between the two constrained nodes. When friction is absent, the line of action of $\mathbf{f}$ has no offset l from the hinge center.

We assume the revolute joint to have no freeplay, so that $R_p - R$ is negligible. Under these assumptions, an ideal revolute constraint without friction between two bodies can be specified by the constraint equations

$$\mathbf{b}_3\mathbf{b}_1 = 0 \tag{5a}$$

$$\mathbf{b}_3\mathbf{b}_2 = 0, \tag{5b}$$

where $\mathbf{b}_1 = \mathbf{R}_b\mathbf{i}_1$, $\mathbf{b}_2 = \mathbf{R}_b\mathbf{i}_2$, and $\mathbf{b}_3 = \mathbf{R}_a\mathbf{i}_3$, with $\mathbf{i}_1 = \{1;0;0\}$, $\mathbf{i}_2 = \{0;1;0\}$, and $\mathbf{i}_3 = \{0;0;1\}$ corresponding to the unit vectors along local coordinate axes 1, 2, and 3, respectively. Equations (5) impose that axes $\mathbf{b}_2$ and $\mathbf{b}_1$ of body b remain perpendicular to the joint axis $\mathbf{b}_3$ of body a.

The Lagrange multipliers associated with a frictionless joint represent a reaction force $\mathbf{r}$ and a reaction moment with components about the two directions normal to the joint axis, $\mathbf{m} = m_1\mathbf{b}_1 + m_2\mathbf{b}_2$. At this stage, we assume the reaction moment $\mathbf{m}$ to be null and the reaction force $\mathbf{r}$ to be normal to the joint axis, i.e., a planar joint; this restriction will be relaxed later. We further assume the joint to be lightly loaded, so that the actual distribution of contact pressure along the circumference, otherwise dependent on both geometric tolerances and load magnitude, can be neglected[5].

[5]Some papers, e.g., [21], suggest that one should account for the distribution of the contact pressure as soon as the load increases. However, they typically use the Hertzian contact pressure distribution, whose limit of validity is precisely that of lightly loaded joint, and that is not accurate, if meaningful at all, for highly loaded joint and conforming contacts such as perfectly fitting pins in an hole. The authors think that,

So far, in this section, ideal constraints have been considered. When friction is introduced, the involved constraints become non-ideal, namely, the corresponding constraint reactions do (virtual) work for a virtual displacement that results in relative motion between the constrained nodes. In the proposed formulation, friction is introduced by augmenting the constraint reactions with tangential friction components expressed through additional unknowns. The following sections discuss this aspect in detail: Sect. 3 for the revolute joint, and Sect. 4 for the spherical joint.

3 Revolute Joint

3.1 Friction Modeling in Revolute Joints

When the joint exhibits friction, the offset l can be nonzero. The transmitted reaction force at the contact point can be decomposed into a normal (or radial) component $\mathbf{r}_n$ and a tangential component $\mathbf{r}_f$, with $\|\mathbf{r}_f\| = f\,\|\mathbf{r}_n\|$, where f is the friction coefficient. The resulting friction-induced moment exchanged between the two bodies is $m = \|\mathbf{r}_f\|\,R = \|\mathbf{r}\|\,l$. Since the bodies are allowed only relative angular velocity aligned with the joint axis, $\boldsymbol{\omega}_r = \boldsymbol{\omega}_a - \boldsymbol{\omega}_b = \omega_r \mathbf{b}_3$, with $\omega_r = \boldsymbol{\omega}_r \mathbf{b}_3$, the direction of the friction-induced moment is known a priori and coincides with that of the joint axis, $\mathbf{m} = m\mathbf{b}_3$.

3.1.1 Total Reaction Force as Unknown

A multibody implementation of a revolute joint with friction can therefore be derived from that of an ideal joint without friction, where the overall joint reaction force $\mathbf{r}$ is obtained as the Lagrange multiplier associated with the constraint enforcing coincidence of the pin and bore centers. In this case, adding friction amounts to computing the friction coefficient f and the corresponding friction-induced moment, aligned with $\mathbf{b}_3$, as $m = f\,\|\mathbf{r}_n\|\,R$. However, since $\|\mathbf{r}_f\| = f\,\|\mathbf{r}_n\|$, the overall reaction force magnitude is given by $\|\mathbf{r}\| = \sqrt{\|\mathbf{r}_n\|^2 + \|\mathbf{r}_f\|^2} = \|\mathbf{r}_n\|\,\sqrt{1+f^2}$, so that one can compute the friction-induced moment as

$$m = \frac{f}{\sqrt{1+f^2}}\,\|\mathbf{r}\|\,R, \tag{6}$$

with the correct sign embedded in the friction coefficient f, and introduce this moment into the joint by applying it, with opposite sign, to the two bodies, without any other modification to the code.

One may argue that, for an admittedly high friction value, e.g., $|f| \geq 0.3$, Eq. (6) implies correcting the friction moment that would be obtained by (incorrectly) using the magnitude of the overall reaction force, $m = f\,\|\mathbf{r}\|\,R$, by only about 5%. Such a difference is likely well within the experimental uncertainty expected in the measurement of the friction coefficient. Nevertheless; this does not make neglecting the increase

in such cases, one should resort to a proper treatment for the conformal contact, see e.g., [22] Section 5.3, to properly account for the contact pressure distribution.

in the magnitude of the overall reaction force due to the presence of the tangential component $\mathbf{r}_f$ conceptually correct.

3.1.2 Normal Reaction Force as Unknown

An alternative approach consists in leaving the frictionless joint equations unchanged, but interpreting the joint reaction force unknowns as the normal component $\mathbf{r}_n$, rather than as the total reaction force. This allows the corresponding friction-induced tangential component

$$\mathbf{r}_f = f\mathbf{r}_n \times \mathbf{b}_3 \tag{7}$$

(where $(\cdot)\times$ denotes the skew-symmetric matrix operator, such that matrix $\mathbf{a}\times$, multiplied by vector $\mathbf{b}$, yields the vector cross-product $\mathbf{a} \times \mathbf{b}$), again with the correct sign embedded in the friction coefficient f, to be computed directly as a function of f, $\mathbf{r}_n$, and the joint axis direction $\mathbf{b}_3$, together with the associated friction-induced moment

$$\mathbf{m} = f \left\|\mathbf{r}_n\right\| R\mathbf{b}_3. \tag{8}$$

By applying the overall reaction force $\mathbf{r} = \mathbf{r}_n + \mathbf{r}_f$, both the joint constraints and the equilibrium equations remain satisfied. As an additional benefit, this latter approach readily identifies the position of the contact point, defined by the angle θ in Fig. 1 resulting from the joint reaction force $\mathbf{r}_n$.

When integrating the constrained problem using an implicit time-stepping scheme, the two approaches are equivalent at convergence, but lead to significantly different linearizations of the forces and moments applied to the constrained bodies.

3.2 Axial Component of Reaction Force

Whenever the joint reaction force is aligned with the hinge axis $\mathbf{b}_3$, $\mathbf{r}_n = r_3\mathbf{b}_3$, the contact does not occur between the two cylindrical surfaces of Fig. 1, i.e., between the knuckles and the pin. Rather, it occurs over the circular ring at the interface between two knuckles (or over any washer interposed between them), see Fig. 2.

Assuming uniform contact pressure all over the circular ring, the resultant of the friction shear is null, and the effect of friction is limited to the friction-induced moment $m_3 = f \left\|\mathbf{r}\right\| R_{\text{equiv}}$. The equivalent radius R_{equiv} can be computed as a function of the inner and outer radii of the contact ring, R_1 and R_2. Assuming the friction coefficient f to be constant all over the contact surface A and the contact pressure p to be inversely proportional to the radial position, $p \propto 1/r$, as is required to have uniform wear over the annular contact surface, one gets

$$R_{\text{equiv}} = \frac{m_3}{fr_3} = \frac{\int_A rpf \ \mathrm{d}A}{f \int_A p \ \mathrm{d}A} = \frac{R_1 + R_2}{2}. \tag{9}$$

3.3 Concluding Remarks

It is worth noting that both Eqs. (7) and (8) hold valid. In the axial component case, Eq. (7) yields $\mathbf{r}_f \equiv \mathbf{0}$ while Eq. (8) requires that the correct radius and the corresponding reaction force component are used for the computation of the moment.

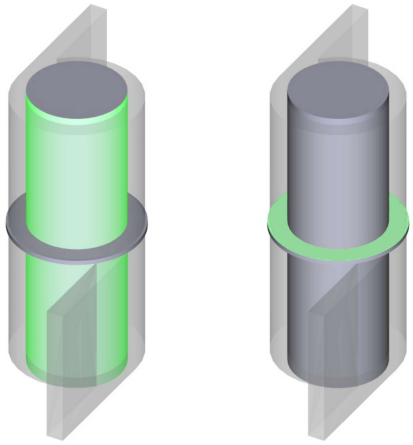

Fig. 2: Reaction force normal to $\mathbf{b}_3$, with contact on the pin (left, contact surface highlighted) and along $\mathbf{b}_3$, with contact between the two knuckles (right, contact surface highlighted).

Table 1: Options accounting for different contact surfaces.

	Projector	Friction arm	Friction force $\mathbf{r}_f$	Friction moment m
Whole reaction (no decomposition)	$\mathbf{I}$	R	$f\mathbf{r}_n \times \mathbf{b}_3$	$f\,\|\mathbf{r}_n\|\,R\mathbf{b}_3$
Axial reaction	$\mathbf{P}_a = \mathbf{b}_3 \otimes \mathbf{b}_3$	R_{equiv}	$\overbrace{f(\mathbf{P}_a\mathbf{r}_n) \times \mathbf{b}_3}^{=\mathbf{0}^a}$	$f\,\|\mathbf{P}_a\mathbf{r}_n\|\,R_{\text{equiv}}\mathbf{b}_3$
Normal (radial) reaction	$\mathbf{P}_n = \mathbf{I} - \mathbf{b}_3 \otimes \mathbf{b}_3 = \mathbf{I} - \mathbf{P}_a$	R	$f(\mathbf{P}_n\mathbf{r}_n) \times \mathbf{b}_3$	$f\,\|\mathbf{P}_n\mathbf{r}_n\|\,R\mathbf{b}_3$

[a] Since $\mathbf{P}_a\mathbf{r}_n$ produces a vector aligned with $\mathbf{b}_3$.

The two cases can be dealt with by decomposing the reaction force $\mathbf{r}_n$ into components aligned with and normal to $\mathbf{b}_3$, possibly by resorting to the axial projector $\mathbf{P}_a = \mathbf{b}_3 \otimes \mathbf{b}_3$, and its complement, the normal projector $\mathbf{P}_n = \mathbf{I} - \mathbf{b}_3 \otimes \mathbf{b}_3 = \mathbf{I} - \mathbf{P}_a$. The options are summarized in Table 1.

When the reaction force has non-zero axial ($\mathbf{P}_a\mathbf{r} \neq \mathbf{0}$) and normal ($\mathbf{P}_n\mathbf{r} \neq \mathbf{0}$) components, the friction moment is a combination of both contributions.

3.4 Revolute Joint Friction Models

Both strategies sketched in Section 3 for the implementation of a revolute joint with friction require the computation of the friction coefficient. Two friction models are considered: an ideal Coulomb friction model and a modified LuGre model.

3.4.1 Coulomb Friction Model

The Coulomb friction model adds a scalar equation to the set of equations of the multibody model; accordingly, the friction coefficient f is added to the set of (algebraic) unknowns. The model keeps track of an internal logic state, which can assume the values *stick* or *slip*.

Stick State.

When the friction model is in the *stick* state, the additional (non-holonomic kinematic constraint) equation enforces null relative velocity between the two bodies at the contact point, namely

$$\phi_{\text{stick}} = v_{\text{rel}} = 0, \tag{10}$$

where v_{rel} is the relative velocity at the contact point,

$$v_{\text{rel}} = R\,(\boldsymbol{\omega}_a - \boldsymbol{\omega}_b)\,\mathbf{b}_3 = R\omega_r. \tag{11}$$

At convergence, the unknown friction coefficient f takes whatever value is required to satisfy Eq. (10).

Slip State.

When the friction model is in the *slip* state, instead, the friction coefficient f is computed using an arbitrarily prescribed velocity-dependent Stribeck curve $\tilde{f}(v_{\text{rel}})$, a function of the relative velocity at the point of contact.

To preserve the dimension and ordering of the nonlinear problem and, more importantly, of the associated Jacobian matrix, Eq. (10) is replaced by the trivial equation

$$\phi_{\text{slip}} = f - \tilde{f}(v_{\text{rel}}) = 0, \tag{12}$$

which defines the friction coefficient f as an algebraic unknown, making the DAE problem's index equal to one if Eq. (12) were the only algebraic equation of the problem. Consequently, the definition of the friction contribution to the reaction force remains the same.

In both cases, regardless of whether the friction model is in the stick or slip state, the sign of the friction coefficient defines the direction of the friction-induced moment, as mentioned earlier.

Transition Between States.

When the model is in the stick state, the friction coefficient f can assume any value in the range $\pm \lim_{v\to 0^+} \tilde{f}(v)$. For this reason, specialized solvers for cone-complementarity problems should, in principle, be employed to guarantee convergence of the solution; see, e.g., [23, 24]. The present model instead relies on a standard Newton-Raphson nonlinear solver. Convergence is achieved, although not guaranteed, by means of a custom heuristic that manages the transition between the stick and slip states. This heuristic keeps track not only of the current state, but also of the type of transition occurring between successive Newton-Raphson iterations (e.g., stick-to-slip, or slip-to-stick), using an additional internal state. Further details on the state-switching strategy are beyond the scope of this paper.

3.4.2 Modified LuGre Model

The modified LuGre friction model, based on the one proposed in [25], is briefly recalled here. A further internal state z is introduced, complemented by the additional differential equation

$$\dot{z} = v_{\mathrm{rel}} \left(1 - \frac{\alpha(z, v_{\mathrm{rel}})}{z_{ss}(v_{\mathrm{rel}})} \mathrm{sgn}(v_{\mathrm{rel}}) z \right), \tag{13}$$

where

$$z_{ss}(v_{\mathrm{rel}}) = \frac{\tilde{f}(|v_{\mathrm{rel}}|)}{\sigma_0} \tag{14a}$$

$$\alpha(z, v_{\mathrm{rel}}) = \left\{ \begin{array}{cc} 0 & |z| < z_{ba} \\ \alpha_m(z, v_{\mathrm{rel}}) & z_{ba} < |z| < z_{ss}(v_{\mathrm{rel}}) \\ 1 & |z| \geq z_{ss}(v_{\mathrm{rel}}) \end{array} \right\} \mathrm{sgn}(v_{\mathrm{rel}}) = \mathrm{sgn}(z) \qquad 0 \quad \mathrm{sgn}(v_{\mathrm{rel}}) \neq \mathrm{sgn}(z) \tag{14b}$$

$$\alpha_m(z, v_{\mathrm{rel}}) = \frac{1}{2} \left[\sin \left(\pi \frac{z - \dfrac{z_{ss}(v_{\mathrm{rel}}) + z_{ba}}{2}}{z_{ss}(v_{\mathrm{rel}}) - z_{ba}} \right) + 1 \right], \tag{14c}$$

with $z_{ba} = k z_{ss}$, i.e., the parameter z_{ss}, which can be interpreted as the "steady-state" value of z, is scaled by a factor $0 < k < 1$. The friction coefficient is defined as

$$f = \sigma_0 z + \sigma_1 \dot{z} + \sigma_2 v_{\mathrm{rel}}. \tag{15}$$

The coefficients σ_0, σ_1, σ_2, and k, as well as the Stribeck curve $\tilde{f}(v_{\mathrm{rel}})$, are defined by the user[6].

Unlike the traditional LuGre model, the introduction of the function α of Eq. (14b) eliminates plastic pre-sliding and guarantees purely elastic pre-sliding behavior with stiffness σ_0 for small relative displacements.

Unlike the Coulomb model, the LuGre one explicitly accounts for stick/slip transition dynamics. However, reasonable estimates of the coefficients may be difficult to obtain without a dedicated experimental identification. In the absence of such tests, increasing the stiffness σ_0 reduces the pre-sliding relative displacement and makes the model increasingly similar to Coulomb friction, at the cost of increased problem stiffness, requiring smaller steps for numerical integration.

3.4.3 Friction Models Interface

In the current MBDyn implementation, both friction models share the same interface. They take as input the current values of their internal states and the relative sliding velocity v_{rel}, append a friction equation to the problem (either of Eqs. (10) or (12) for the Coulomb model, or Eq. (13) for the LuGre model), and provide the value of the friction coefficient f as a variable in the algebraic subset.

[6] In the proposed implementation, the user is requested to define the constants σ_0, σ_1, σ_2, and k, and the Stribeck curve as a function of the relative velocity. Then z_{ss} is computed internally as $z_{ss} = \tilde{f}(|v_{\mathrm{rel}}|)/\sigma_0$, and z_{ba} as $z_{ba} = k z_{ss}$.

If required, both models can compute the derivatives of the governing equations and of the friction coefficient with respect to their internal states and the relative sliding velocity. This information is sufficient to transparently interface the friction models with the revolute joint.

4 Spherical Joint

4.1 Friction Modeling in Spherical Joints

The literature on friction modeling in spherical joints is less extensive than that on planar and revolute contacts. In what is perhaps one of the first contributions, Smirnov [26] assumes that the distribution of the normal contact pressure p over the contact region is axisymmetric about the center of the contact region itself and is given by

$$p = p_0 \cos\left(\frac{\alpha}{\alpha_0}\frac{\pi}{2}\right), \tag{16}$$

where α is the angle between the unit vector $\mathbf{n}$, aligned with the resultant of the contact pressure, and the point at which the contact pressure is evaluated. The angle α_0 depends, in principle, on the transmitted load.

The integration of the pressure distribution over the contact surface yields the resultant normal contact force component r_n. Additional surface integrals compute, as functions of the normal resultant $r_n\mathbf{n}$, of:

1. the resultant of the friction shear stresses $\mathbf{r}_f$,
2. the so-called moment of slip friction $\mathbf{m}_f = m_f\mathbf{n} \times \boldsymbol{\omega}_r/|\boldsymbol{\omega}_r|$, which is orthogonal to both $\mathbf{n}$ and the relative angular velocity $\boldsymbol{\omega}_r = (\boldsymbol{\omega}_a - \boldsymbol{\omega}_b)$, and
3. the moment of rotational friction $\mathbf{m}_n = m_n\mathbf{n}$, which is aligned with the normal direction $\mathbf{n}$.

Smirnov's formulae, reported without any derivation in [26], were carefully re-derived and validated in [27]. In that work, considerable effort is devoted to computing the direction $\mathbf{n}$ as a function of the overall transmitted force $\mathbf{r} = \mathbf{r}_n + \mathbf{r}_f$, the friction coefficient, and the relative angular velocity $\boldsymbol{\omega}_r$, to incorporate frictional effects within a multibody formulation in which the joint unknowns represent the total reaction force. The resulting expressions are rather involved and cannot be evaluated in closed form, requiring the solution of a nonlinear problem to compute the friction-induced moments as functions $\mathbf{r}$, $\boldsymbol{\omega}_r$, and of the friction coefficient f.

While the friction moment in a hinge joint is by definition a priori about the joint axis, a spherical joint's friction moment direction is an unknown that must be resolved as part of the system equilibrium. Moreover, the expressions for the direction $\mathbf{n}$ as a function of the overall reaction force $\mathbf{r}$ as derived in [27] require a nonzero relative angular velocity $\boldsymbol{\omega}_r \neq \mathbf{0}$, which precludes their use in the stick regime, and may lead to convergence issues near the stick-slip transition.

Finally, when the joint is slightly loaded, the contact angle α_0 is typically small, and the pressure distribution can be reasonably approximated as uniform. This situation

also arises in straddle-type joints (spherical bearings) predominantly loaded in the radial direction. For small α_0, the moment arm of the friction shear stresses is small, and the rotational friction moment m_r is often negligible compared to the slip friction moment m_s.

4.2 Proposed Spherical Joint Friction Formulation

In the following, a formulation is proposed that mirrors the hinge joint approach based on the normal transmitted force. Specifically, the formulation:

- assumes a lightly loaded joint, allowing the contact pressure distribution to be neglected;
- neglects the moment of rotational friction m_r, which would otherwise require detailed modeling of the contact area and integration of the contact shear stress moment;
- models both the friction shear resultant $\mathbf{r}_f$ and the moment of slip friction $\mathbf{m}_f$ as functions of the normal reaction force $\mathbf{r}_n$ and of the friction coefficient, assuming both lie in the plane normal to the direction $\mathbf{n}$ (i.e., tangent to the surface of the sphere), $\mathbf{I} - \mathbf{n} \otimes \mathbf{n}$;
- interprets the joint reaction force unknowns as the normal component $\mathbf{r}_n$, rather than the total reaction force $\mathbf{r}$, thereby significantly simplifying the formulation;
- allows for a transparent treatment of the stick regime.

As a counterpart, since the relative angular velocity $\boldsymbol{\omega}_r$ is not used to define a local reference system, and since the formulation must remain valid in the stick regime, a local coordinate system must be introduced for any admissible direction $\mathbf{n}$ of the normal reaction force. This local system is required to express the two tangential components of both the friction shear stress resultant $\mathbf{r}_f$ and the moment of slip friction $\mathbf{m}_f$, and to track any vector-valued internal states of the friction models.

In principle, a natural local reference system can be determined during the slip phase by considering the direction of the relative velocity between the two parts at the point of contact as the principal tangent direction, $\mathbf{t}_{v_{\text{rel}}} = \mathbf{v}_{\text{rel}}/\|\mathbf{v}_{\text{rel}}\|$, with the other tangent direction given by $\mathbf{t}_{\text{lat}} = \mathbf{n} \times \mathbf{t}_{v_{\text{rel}}}$. Similarly, a natural local reference system could be identified during the stick phase by considering, as the principal tangent direction, that of the tangent component of the friction shear stresses' resultant. However, both approaches would make the problem far more "implicit" than strictly necessary.

Instead, a local reference system is defined at the point of contact, consisting of a unit vector $\mathbf{n}$ normal to the contact surfaces at the contact point and two mutually orthogonal unit vectors $\mathbf{t}_1$ and $\mathbf{t}_2$ tangent to the contact surface. The latter are arbitrarily initialized and their evolution, as the contact point moves, is tracked by minimizing the rotation from the corresponding unit vectors at the previous time step, as discussed later in Sec. 4.4.

The overall joint internal force $\mathbf{r}$ is decomposed into a component normal to the point of contact, r_n, in direction $\mathbf{n}$, and two tangential components in directions $\mathbf{t}_1$ and $\mathbf{t}_2$. The latter are proportional to r_n and to the corresponding friction coefficients,

f_1 and f_2, namely

$$\mathbf{r}_f = r_n(f_1\mathbf{t}_1 + f_2\mathbf{t}_2). \tag{17}$$

An arbitrary friction-induced moment $\mathbf{m}$ can then be decomposed as $\mathbf{m} = m_n\mathbf{n} + m_1\mathbf{t}_1 + m_2\mathbf{t}_2$, where the moment of slip friction $\mathbf{m}_f = m_1\mathbf{t}_1 + m_2\mathbf{t}_2$ can readily be computed as

$$\mathbf{m}_f = (R\mathbf{n}) \times (r_n f_1\mathbf{t}_1 + r_n f_2\mathbf{t}_2) = Rr_n(f_1\mathbf{t}_2 - f_2\mathbf{t}_1). \tag{18}$$

where the radius R is the distance of the spheres' contact surfaces from their common center. Two friction coefficients are required instead of a scalar value because the relative velocity vanishes in the stick regime.

The initial directions for the unit vectors $\mathbf{t}_1$ and $\mathbf{t}_2$ can be constructed whenever the normal reaction force is nonzero using the procedure described in Appendix A; their evolution must be continuously tracked in time, avoiding singularities associated with finite rotation parametrization, as described in Section 4.4. When the reaction force becomes sufficiently small (i.e., its magnitude falls below a prescribed threshold), friction becomes negligible; when it reappears, the process is reinitialized.

4.3 Spherical Joint Friction Moment

Two friction models are considered: a two-dimensional Coulomb model and a two-dimensional modified LuGre model. Both models receive as input the components v_1 and v_2 of the relative sliding velocity[7] at the point of contact, such that

$$\mathbf{v}_{\text{rel}} = v_1\mathbf{t}_1 + v_2\mathbf{t}_2, \tag{19}$$

and provide the friction coefficients in directions $\mathbf{t}_1$ and $\mathbf{t}_2$, namely f_1 and f_2. To do so, they both introduce two friction-related equations, detailed in Secs. 4.3.1 and 4.3.2, that must be solved along with the rest of the problem.

The tangential components of the relative velocity $\mathbf{v}_{\text{rel}} = \boldsymbol{\omega}_{\text{rel}} \times (R\mathbf{n})$ are obtained as $v_1 = \mathbf{t}_1 \cdot \mathbf{v}_{\text{rel}}$ and $v_2 = \mathbf{t}_2 \cdot \mathbf{v}_{\text{rel}}$.

4.3.1 Two-Dimensional Coulomb Friction Model

The generalization of the Coulomb friction model of Sect. 3.4.1 to two dimensions introduces two scalar equations and two scalar unknowns, f_1 and f_2, representing the friction coefficients in directions $\mathbf{t}_1$ and $\mathbf{t}_2$, respectively. The friction shear resultant is thus that of Eq. (17).

The model uses the internal states and stick-slip transition logic discussed for the one-dimensional case to deal with the stick and slip conditions and allows to successfully converge to a solution.

[7] It is worth noticing that here $\mathbf{v}_{\text{rel}}$ is a three-dimensional vector, as $\mathbf{t}_1$ and $\mathbf{t}_2$ are. However, having assumed continuous contact of the parts, its component along $\mathbf{n}$ is always zero. In subsequent sections, the same symbol $\mathbf{v}_{\text{rel}}$ is used to indicate the projection of the three-dimensional relative velocity vector on the tangent space. No ambiguity is possible considering the context in which $\mathbf{v}_{\text{rel}}$ is used.

In the stick regime, the two equations enforce null sliding velocity,

$$\boldsymbol{\phi}_{\text{stick}} = \left\{ \begin{array}{c} v_1 \\ v_2 \end{array} \right\} = \mathbf{v}_{\text{rel}} = \mathbf{0}, \tag{20}$$

where $\mathbf{v}_{\text{rel}}$ now refers to the two-dimensional vector in the tangent plane at the point of contact, and the friction coefficients f_1 and f_2, collected in vector $\mathbf{f}$, take whatever value is required to satisfy this condition, provided that $\|\mathbf{f}\| = \sqrt{f_1^2 + f_2^2} \leq \lim_{\|\mathbf{v}_{\text{rel}}\| \to 0^+} \tilde{f}(\|\mathbf{v}_{\text{rel}}\|)$.

In the slip regime, the friction force is assumed to act opposite to the sliding velocity direction, with magnitude given by the scalar Stribeck curve $\tilde{f}(\|\mathbf{v}_{\text{rel}}\|)$, so that

$$\boldsymbol{\phi}_{\text{slip}} = \mathbf{f} + \tilde{f}(\|\mathbf{v}_{\text{rel}}\|) \frac{\mathbf{v}_{\text{rel}}}{\|\mathbf{v}_{\text{rel}}\|} = \mathbf{0}. \tag{21}$$

The stick-slip transition logic and internal state handling are identical to those discussed for the one-dimensional case.

4.3.2 Modified Two-Dimensional LuGre Model

The generalization of the modified LuGre friction model of Sect. 3.4.2 to two dimensions follows the formulation proposed in [28]. Two internal states z_1 and z_2, collected in vector $\mathbf{z}$, are introduced, together with two friction coefficients f_1 and f_2, collected in vector $\mathbf{f}$.

The dynamics of the internal states $\mathbf{z}$ are defined by

$$\dot{\mathbf{z}} = \mathbf{v}_{\text{rel}} - \frac{\alpha(\mathbf{z}, \mathbf{v}_{\text{rel}})}{z_{ss}(\|\mathbf{v}_{\text{rel}}\|)} \mathbf{z} \|\mathbf{v}_{\text{rel}}\|, \tag{22}$$

where

$$z_{ss}(\|\mathbf{v}_{\text{rel}}\|) = \tilde{f}(\|\mathbf{v}_{\text{rel}}\|)/\sigma_0 \tag{23a}$$

$$\alpha(\mathbf{z}, \mathbf{v}_{\text{rel}}) = \tilde{\alpha}(\|\mathbf{z}\|, \|\mathbf{v}_{\text{rel}}\|) \varepsilon(\mathbf{z}, \mathbf{v}_{\text{rel}}) \tag{23b}$$

$$\varepsilon(\mathbf{z}, \mathbf{v}_{\text{rel}}) = \frac{1}{2} \left(\frac{\mathbf{v}_{\text{rel}}}{\|\mathbf{v}_{\text{rel}}\|} \cdot \frac{\mathbf{z}}{\|\mathbf{z}\|} + 1 \right)$$

$$\tilde{\alpha}(\|\mathbf{z}\|, \|\mathbf{v}_{\text{rel}}\|) = \left\{ \begin{array}{ll} 0 & \|\mathbf{z}\| < z_{ba} \\ \alpha_m(\|\mathbf{z}\|, \|\mathbf{v}_{\text{rel}}\|) & z_{ba} < \|\mathbf{z}\| < z_{ss}(\|\mathbf{v}_{\text{rel}}\|) \\ 1 & \text{otherwise} \end{array} \right. \tag{23c}$$

$$\alpha_m(\|\mathbf{z}\|, \|\mathbf{v}_{\text{rel}}\|) = \frac{1}{2} \left[\sin \left(\pi \frac{\|\mathbf{z}\| - \frac{z_{ss}(\|\mathbf{v}_{\text{rel}}\|) + z_{ba}}{2}}{z_{ss}(\|\mathbf{v}_{\text{rel}}\|) - z_{ba}} \right) + 1 \right], \tag{23d}$$

and $z_{ba} = kz_{ss}$ as for the 1D case. When either $\|\mathbf{v}_{\text{rel}}\| \to 0$ or $\|\mathbf{z}\| \to 0$, then $\varepsilon \to 1$ (to be more precise, when they fall below a prescribed threshold, ε is set to 1)[8].

The friction coefficient vector is finally defined as

$$\mathbf{f} = \sigma_0 \mathbf{z} + \sigma_1 \dot{\mathbf{z}} + \sigma_2 \mathbf{v}_{\text{rel}} \tag{25}$$

through a generalization of Eq. (15).

4.4 Spherical Joint Local Coordinate System

As explained in Sec. 4.2, the two-dimensional friction model requires two mutually orthogonal unit vectors, $\mathbf{t}_1$ and $\mathbf{t}_2$, on the plane defined by the normal reaction force direction $\mathbf{n}$. At the beginning of the simulation, or whenever the contact point has a significant discontinuity, these vectors can be initialized by following the procedure detailed in Appendix A.

While the algorithm of Appendix A defines a local reference system at the contact point, it is convenient that this reference system varies smoothly as $\mathbf{n}$ changes. This is required to consistently integrate with respect to time and linearize friction models (e.g., the modified two-dimensional LuGre model of Section 4.3.2) that introduce vector-valued internal states defined in the local frame.

Let the local reference system at the previous step be defined by $\tilde{\mathbf{n}}$, $\tilde{\mathbf{t}}_1$ and $\tilde{\mathbf{t}}_2$. Given the updated normal vector $\mathbf{n}$, a rotation tensor $\mathbf{R} \in \text{SO}(3)$ is sought such that $\mathbf{n} = \mathbf{R}\tilde{\mathbf{n}}$, and $\mathbf{t}_1 = \mathbf{R}\tilde{\mathbf{t}}_1$ and $\mathbf{t}_2 = \mathbf{R}\tilde{\mathbf{t}}_2$. While the plane in which $\mathbf{t}_1$ and $\mathbf{t}_2$ lie is uniquely defined as that of normal $\mathbf{n}$, there are infinite combinations of $\mathbf{t}_1$ and $\mathbf{t}_2$ that satisfy the only requirements of being mutually orthogonal and orthogonal to $\mathbf{n}$, forming a right-hand triad. They differ by an arbitrary rotation about $\mathbf{n}$. Among these infinite rotations, that of minimal rotation angle,

$$\theta = \arccos(\tilde{\mathbf{n}} \cdot \mathbf{n}) \,, \tag{26}$$

and rotation axis

$$\mathbf{k} = \frac{\tilde{\mathbf{n}} \times \mathbf{n}}{\|\tilde{\mathbf{n}} \times \mathbf{n}\|} \text{ (if } \tilde{\mathbf{n}} \neq \pm\mathbf{n}) \tag{27}$$

is selected. Using Rodrigues' rotation formula, the rotation tensor $\mathbf{R}$ is

$$\mathbf{R} = \mathbf{I} + \sin\theta\, \mathbf{k}\times + (1 - \cos\theta)\, \mathbf{k}\times\mathbf{k}\times \,. \tag{28}$$

This rotation tensor $\mathbf{R}$ minimizes the rotation vector norm (i.e., uses the smallest angle θ) while satisfying $\mathbf{R}\tilde{\mathbf{n}} = \mathbf{n}$.

---

[8] In simple words, ε is 1/2 plus half the inner product of the unit vectors associated with $\mathbf{v}_{\text{rel}}$ and $\mathbf{z}$, namely half the cosine of the angle they form. If we call

$$\cos\vartheta = \frac{\mathbf{v}_{\text{rel}}}{\|\mathbf{v}_{\text{rel}}\|}\frac{\mathbf{z}}{\|\mathbf{z}\|} \tag{24}$$

then $\varepsilon = (1+\cos\vartheta)/2$. As such, ε can vary with continuity between 0 and 1. The vanishing of the magnitude of either vector (or of both) is considered equivalent to their directions becoming orthogonal.

Two special cases are handled explicitly. In the parallel case, the two vectors are coincident, $\tilde{\mathbf{n}} = \mathbf{n}$, thus $\theta = 0$ and $\mathbf{R} = \mathbf{I}$. In the antiparallel case, $\tilde{\mathbf{n}} = -\mathbf{n}$; thus, a rotation by $\theta = \pi$ around an arbitrary axis normal to $\tilde{\mathbf{n}}$ can bring it into $\mathbf{n}$. We arbitrarily choose $\tilde{\mathbf{t}}_1$ as such axis. To guarantee numerical stability, vectors are considered parallel/antiparallel whenever $\tilde{\mathbf{n}} \cdot \mathbf{n} \approx \pm 1$.

Knowing $\mathbf{R}$ as a function of $\mathbf{n}$ (with $\tilde{\mathbf{n}}$ given) makes it possible to compute $\mathbf{t}_1$ and $\mathbf{t}_2$ as functions of $\mathbf{n}$ (with $\tilde{\mathbf{t}}_1$ and $\tilde{\mathbf{t}}_2$ given). The linearization is straightforward: the virtual rotation vector $\boldsymbol{\varphi}_\delta\times = \delta\mathbf{R}\mathbf{R}^T$ by design has, when evaluated for $\mathbf{R} = \mathbf{I}$, only components along $\tilde{\mathbf{t}}_1$ and $\tilde{\mathbf{t}}_2$. Because the minimum-angle rotation is selected, its incremental rotation vector has no component about $\tilde{\mathbf{n}}$. Thus, since by definition $\delta\mathbf{R}\tilde{\mathbf{R}} = \delta\mathbf{R}[\tilde{\mathbf{n}}\,\tilde{\mathbf{t}}_1\,\tilde{\mathbf{t}}_2] = [\delta\mathbf{n}\,\delta\mathbf{t}_1\,\delta\mathbf{t}_2]$ and $\delta\mathbf{n} = \delta n_1\tilde{\mathbf{t}}_1 + \delta n_2\tilde{\mathbf{t}}_2$, with a bit of manipulation one gets

$$\delta\mathbf{t}_1 = -\tilde{\mathbf{n}} \otimes \tilde{\mathbf{t}}_1 \cdot \delta\mathbf{n}, \tag{29a}$$

$$\delta\mathbf{t}_2 = -\tilde{\mathbf{n}} \otimes \tilde{\mathbf{t}}_2 \cdot \delta\mathbf{n}. \tag{29b}$$

5 Numerical Results

5.1 Revolute Joint

This section presents a simple revolute joint and a triple pendulum, modeled using revolute joints with friction.

5.1.1 Simple Revolute Joint

The first example is meant to verify the correctness of the friction hinge implementation and the equivalence between the joint formulations with the Lagrange multipliers accounting for the whole reaction force or only for its normal component. A node associated with a body of unit mass and inertia tensor equal to $\mathrm{diag}(1, 1, 0.05)$ kg·m^2 is constrained to a second clamped node by a hinge joint with the rotation axis aligned with $\mathbf{i}_3$. Two time-varying forces $\mathbf{f}_1 = 10\sin(60t)\mathbf{i}_1$ N and $\mathbf{f}_2 = 10\cos(25t)\mathbf{i}_2$ N and a time-varying moment $\mathbf{c}_3 = 0.4\sin(70t)\mathbf{i}_3$ N·m are applied to the first node, so that both the direction and the magnitude of the normal reaction force varies with time, with also the applied external couple varying. The Stribeck curve is assumed to be constant, $\tilde{f}(v_{\mathrm{rel}}) = 0.3$, and the parameters of the LuGre model are $\sigma_0 = 2 \cdot 10^6$ m^{-1}, $\sigma_1 = 2.8$ s $\cdot$ m^{-1}, $\sigma_2 = 0$ s $\cdot$ m^{-1}, and $k = 0.71$. They represent illustrative numerical values, chosen to exercise the model and with sufficiently high stiffness to approximate idealized Coulomb behavior. The joint radius is equal to $R = 0.1$ m. As a result, the node keeps switching between stick and sliding states, as shown in Fig. 3.

Table 2 compares the number of iterations required to achieve convergence with a time step of $\Delta t = 10^{-4}$ s using the Coulomb and Lugre friction models and the Lagrange multipliers accounting either for the whole reaction force or only for its normal component. The Coulomb friction model requires more iterations to converge in this test; it should be noted, however, that it often allows to use significantly longer time steps with respect to those required by the LuGre friction model. The two different joint formulations require roughly the same number of iterations, suggesting

Table 2: Revolute joint: iteration comparison

	Coulomb		LuGre	
Iterations	Old	New	Old	New
6	0	0		
5	85	153		
4	1051	370	4	3
3	3254	1531	581	457
2	3788	3233	11251	23867
1	111824	114714	108166	95675

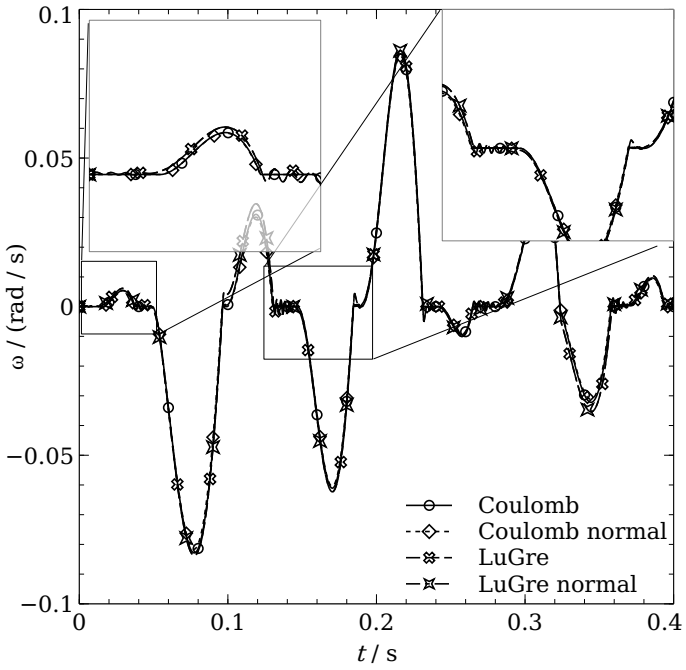

Fig. 3: Revolute joint: relative angular velocity

that the choice of formulation is more of a matter of convenience than of anything else. This is confirmed by the time history of the node's angular velocity, reported in Fig. 3 where, besides minor differences between the two friction models, both joint models give rather similar results. Similar results are also achieved, in this particular case, using both the identity and the normal reaction force projectors, as defined in Table 1.

5.1.2 Triple pendulum

The overall algorithmic robustness and equivalence of the two different joint implementations is further verified by comparing the response of the triple pendulum of

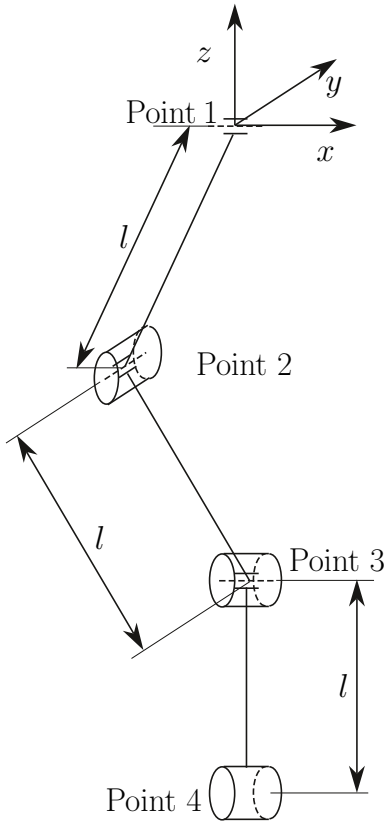

Fig. 4: Revolute joint: triple pendulum linear velocity time histories

Fig. 4. It consists of three rigid bodies, sketched as cylinders in the figure, that are connected by three hinges, the first and the last aligned with the x axis, and the second with the y axis. The offset between the joint and the mass center of gravity is equal to $l = 10$ m; the rigid bodies have unit mass and an inertial tensor equal to $\mathrm{diag}(1, 1, 1)$ kg·m^2. The friction parameters are $\tilde{f}(v_{\mathrm{rel}}) = 0.3$, $\sigma_0 = 2 \cdot 10^5$ m^{-1}, $\sigma_1 = 2.8$ s $\cdot$ m^{-1}, $\sigma_2 = 0$ s $\cdot$ m^{-1}, and $k = 0.71$, and the joint radius is $R = 0.1$ m. Gravity acceleration of magnitude $g = 9.81$ m/s^2 points downward. The system starts from a vertically aligned configuration; at time $t = 0$ s, a single cycle of the force $\mathbf{f} = (10/\sqrt{2}\mathbf{i}_1 + 10/\sqrt{2}\mathbf{i}_2)\sin(60t)$ N is applied to Point 3. Figure 5 compares the trajectories of Point 3 and Point 4 obtained with both friction models and the two joint formulations, confirming also for this somewhat complex and potentially chaotic system the equivalence of the two approaches dealing with friction in this joint.

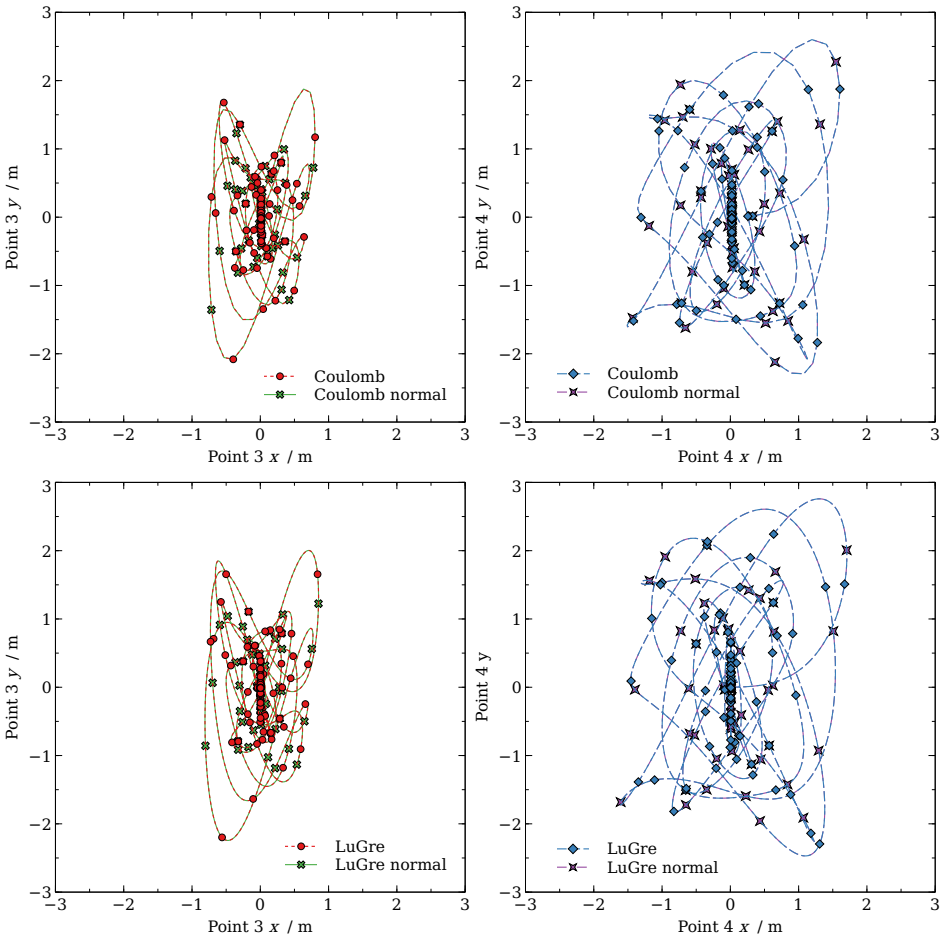

Fig. 5: Revolute joint: triple pendulum Points 3 and 4 trajectories

5.2 Spherical Joint

This section presents a local reference system update example, a simple spherical hinge emulating the simple revolute joint of Sect. 5.1.1, and a spherical pendulum, all modeled using spherical joints with friction.

5.2.1 Local Coordinates Updating

The spherical joint friction formulation depends on the definition and smoothness of the local coordinates defined on the surface following the update strategy of Sec. 4.4. The first test is meant to verify the versatility and robustness of the local coordinate updating strategy.

A node is constrained by a spherical joint to another node that is rigidly connected to the ground. A body of unit mass is associated with the former node. The body's

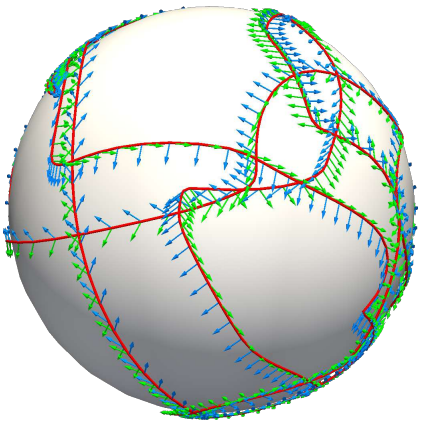

Fig. 6: Spherical joint: local coordinates updating: contact point trajectory and local coordinates.

center of mass is coincident with the node, and its inertia tensor is $\mathrm{diag}(1,1,1)\,\mathrm{kg{\cdot}m^2}$. The joint radius is $R = 1\,\mathrm{m}$. The friction model parameters are $\tilde{f}(v_{\mathrm{rel}}) = 0.3$, $\sigma_0 = 2 \cdot 10^3\,\mathrm{m}^{-1}$, $\sigma_1 = 0.1\,\mathrm{s} \cdot \mathrm{m}^{-1}$, $\sigma_2 = 0\,\mathrm{s} \cdot \mathrm{m}^{-1}$ and $k = 0.71$.

Starting from rest, two external moments $\mathbf{c}_1 = 5\sin(35t)\mathbf{i}_1\,\mathrm{N{\cdot}m}$ and $\mathbf{c}_2 = 1.5\sin(50t)\mathbf{i}_2\,\mathrm{N{\cdot}m}$, and three forces $\mathbf{f}_1 = 5\sin(35t)\mathbf{i}_1\,\mathrm{N}$, $\mathbf{f}_2 = 8\sin(25t)\mathbf{i}_2\,\mathrm{N}$, and $\mathbf{f}_3 = 8\sin(30t)\mathbf{i}_3\,\mathrm{N}$ are applied to the node. The resulting contact point trajectory and the orientation of the local coordinates, $\mathbf{t}_1$ and $\mathbf{t}_2$, are shown in Fig. 6, confirming the capability of the proposed strategy to provide a smooth update along trajectories covering the sphere.

Notice that neither of the local coordinates is aligned with the local velocity, nor are they uniquely defined as functions of the position on the sphere. This is expected; it is not an issue as long as the friction coefficient is not a function, at any given point, of the velocity direction (friction is isotropic[9]).

5.2.2 Simple Spherical Hinge

This example is meant to verify the correctness of the friction implementation and illustrate the stick-slip behavior of the spherical joint. Also in this case, a node is constrained by a spherical joint to another node that is rigidly connected to the ground. A body of unit mass is associated with the former node. The body's center of mass is coincident with the node, and its inertia tensor is $\mathrm{diag}(1,1,0.05)\,\mathrm{kg{\cdot}m^2}$.

Two time-varying forces $\mathbf{f}_1 = 10\sin(60t)\mathbf{i}_1\,\mathrm{N}$ and $\mathbf{f}_2 = 10\cos(25t)\mathbf{i}_2\,\mathrm{N}$, and a time-varying moment $\mathbf{c}_3 = 0.4\sin(70t)\mathbf{i}_3\,\mathrm{N{\cdot}m}$ are applied to the first node. Both the direction and magnitude of the normal reaction force vary with time, with the applied external moment varying as well. The forces lie in the plane normal to axis $\mathbf{i}_3$, and the moment is about the same axis; as such, a planar motion is expected.

[9] In case of non-isotropic friction, one would need to be able to resolve the relative orientation between the local coordinates and a reference orientation defined on the sphere, something that only requires further orientation manipulation but is not otherwise prevented by the proposed formulation.

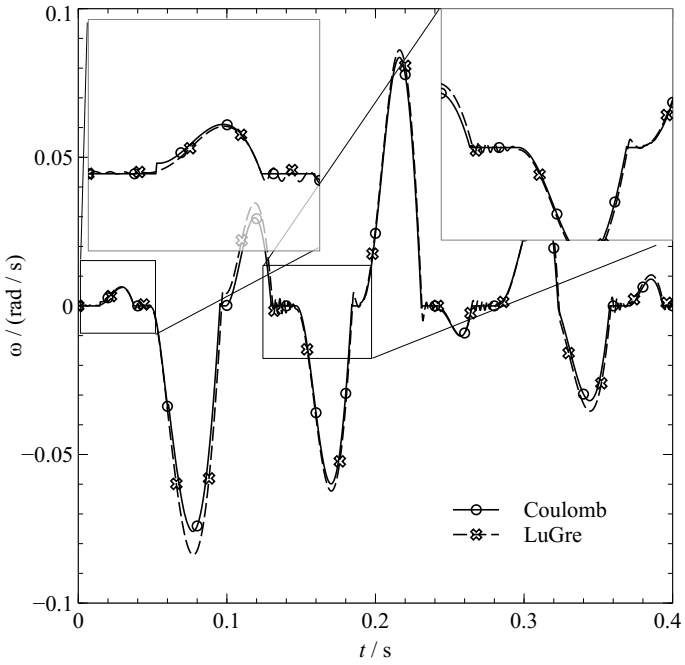

Fig. 7: Spherical joint: relative angular velocity

The Stribeck curve is assumed constant, $\tilde{f}(v_{\text{rel}}) = 0.3$. The parameters of the LuGre model are $\sigma_0 = 2 \cdot 10^6\,\text{m}^{-1}$, $\sigma_1 = 2.8\,\text{s} \cdot \text{m}^{-1}$, $\sigma_2 = 0\,\text{s} \cdot \text{m}^{-1}$, and $k = 0.71$. The radius of the joint is $R = 0.1\,\text{m}$. The resulting motion keeps switching between sticking and slipping, as shown in Fig. 7. During the stick regime, the results of the LuGre model show small oscillations about the rest position, a feature of the model's internal dynamics.

The Coulomb friction model requires more iterations to converge in this test; it should be noted, however, that it often allows to use significantly longer time steps with respect to those required by the LuGre friction model.

5.2.3 Spherical Pendulum

A spherical pendulum has length $l = 10\,\text{m}$, unit mass, and inertia tensor $\text{diag}(1,1,1)\,\text{kg}{\cdot}\text{m}^2$. The gravity acceleration $g = 9.81\,\text{m/s}^2$ points downward. The joint's radius is $R = 0.1\,\text{m}$. The friction parameters are $\tilde{f}(v_{\text{rel}}) = 0.3$, $\sigma_0 = 2 \cdot 10^3\,\text{m}^{-1}$, $\sigma_1 = 0.1\,\text{s} \cdot \text{m}^{-1}$, $\sigma_2 = 0\,\text{s} \cdot \text{m}^{-1}$, and $k = 0.71$. At $t = 0\,\text{s}$, two forces $\mathbf{f}_1 = 10/\sqrt{2}\sin(3t)(\mathbf{i}_1 + \mathbf{i}_2)\,\text{N}$ and $\mathbf{f}_2 = 10\sin(30t)\mathbf{i}_2\,\text{N}$ are applied to the extremity of the pendulum for half period (essentially, a "bump" of $\pi/3$ s) each. Figure 8 shows the resulting trajectory of the pendulum. Since the joint never sticks, essentially the same results are obtained with both the Coulomb and LuGre friction models.

Figure 9 presents the total energy of the overall system, which decreases with time because of the power dissipated through friction. The rate of dissipation is not

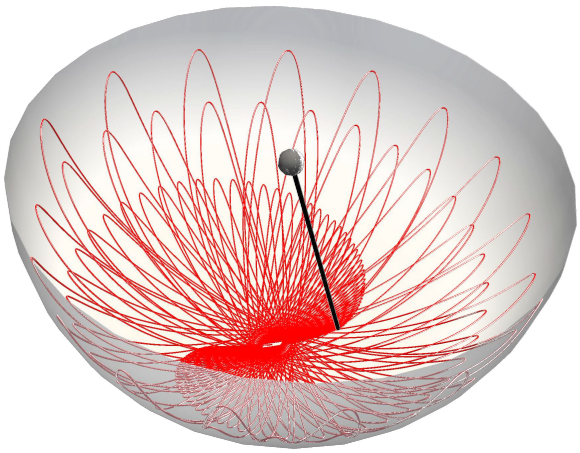

Fig. 8: Spherical joint: pendulum trajectory.

constant, as highlighted in the zoomed portion of the graph, because the joint normal reaction force, to which the friction force is proportional, is not constant. It reaches its maximum when the pendulum passes near the vertical position and has, at the same time, the maximum velocity. At that point, gravity and centrifugal contributions add, the latter being proportional to the square of the velocity.

5.3 Gimbal Joint

The last application is a problem that resembles the artifact that originally motivated this work: the gimbal of Fig. 10. As discussed in [29], friction in the gimbal joint assembly of a tiltrotor wind tunnel model could explain unexpected results in terms of experimentally measured damping during aeroelastic stability tests [30]. The present formulation was developed to represent friction in load-carrying spherical joints in a way that preserves realistic force transmission paths and remains compatible with robust numerical integration of constrained systems like this gimbal joint assembly.

The details of the joint used in the wind-tunnel model are confidential. For this reason, a generic gimbal with similar geometry but different dimensions and load conditions is used here to exemplify the use and the capabilities of the proposed formulation[10]. Key data are presented in Table 3.

A spherical joint at the center of the gimbal assembly connects the hub (indicated as (1) in Fig. 10) to the mast, constraining the three components of the relative position between the two parts. The hub is the only part with non-negligible mass. Its center of mass is at the center of the sphere, thus making the mass irrelevant, with the inertia tensor reported in Table 3.

Three compass assemblies (one of which is indicated as (2) in Fig. 10) ensure robust torque transmission and balanced load distribution. However, from a kinematic

[10]The MBDyn model of the gimbal example is available, from the main git repository of MBDyn, https://public.gitlab.polimi.it/DAER/mbdyn, in folder `tests/joints/spherical/gimbal`.

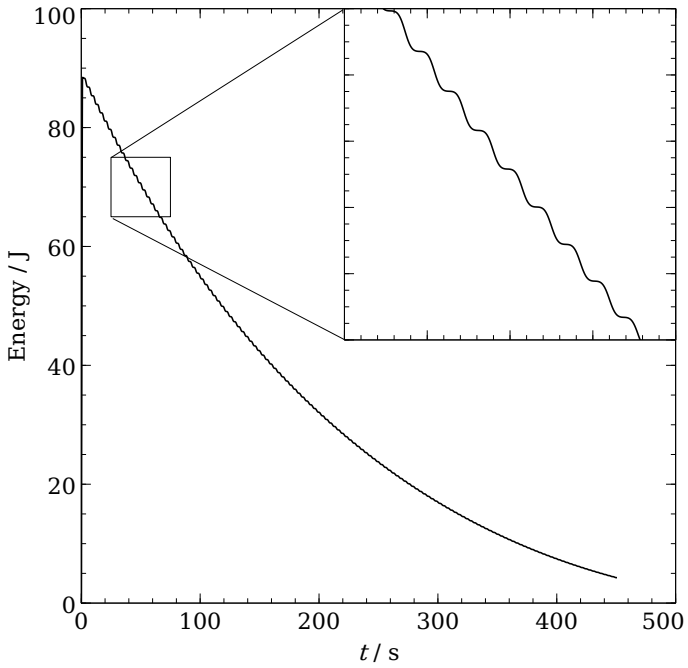

Fig. 9: Spherical joint: pendulum total energy.

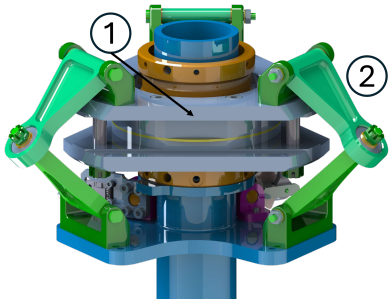

Fig. 10: Gimbal joint: CAD model of a tiltrotor gimbal joint assembly [29].

perspective, a single compass would be sufficient to constrain the system, when modeled using rigid bodies as in the present case. Implementing all three compasses in the numerical model, mandatory to ensure the correct load paths within the parts of the system, creates redundant constraints that would lead to an ill-conditioned mathematical problem.

To overcome this issue, the spherical hinges of the three compasses are modeled using Tikhonov-based constraint regularization. This approach modifies selected

Table 3: Gimbal data.

Reference angular velocity	Ω_{ref}	60	rad/s
Radius of the sphere	R	40	mm
Radial offset of compass revolute hinges		32	mm
Radial offset of compass spherical hinges		64	mm
Axial distance between revolute hinges		80	mm
Hub inertia tensor wrt/ center of mass		$\text{diag}(1, 1, 2)$	kg·m^2
Simplified governor gain	G	100	N·m·s/rad
Friction coefficient	$\tilde{f}(v_{\text{rel}})$	0.7	

constraint equations through the introduction of a compliance coefficient,

$$\phi = 0 \qquad \rightarrow \qquad \phi = c\lambda, \tag{30}$$

with $0 < c \ll 1$, effectively transforming rigid constraints into stiff elastic connections[11]. Mathematically, this can be interpreted as replacing an ideally infinitely stiff constraint with a finite but very large stiffness value.

A regularization compliance value $c = 10^{-11}$ m/N was placed over the compass spherical hinges, carefully tuned to the lowest possible value that maintained numerical stability while minimizing constraint violations. This approach allowed for the realistic representation of the complete compass assembly, including the potential for different friction characteristics in each compass, without creating a numerically intractable over-constrained system.

Representative load conditions are obtained by introducing:

- a constant torque $C_{3_{\text{hub}}} = -C_{\text{ref}}$ on the hub, about its axis and opposite to the angular velocity, representing the rotor's aerodynamic torque; its direction is fixed in the reference system of the hub, and thus follows it when it tilts;
- a corresponding torque on the mast, about its axis and with the same sign of the angular velocity, with superimposed a correction proportional to the difference between the current and the nominal value of the angular velocity, namely $C_{3_{\text{mast}}} = C_{\text{ref}} - G(\omega_{3_{\text{mast}}} - \Omega_{\text{ref}})$, representing the motor torque;
- a torque disturbance on the hub, about its local axis 2, varying harmonically with three times the azimuthal angle of the mast, $C_{2_{\text{hub}}} = C_d \sin(3\psi_{\text{mast}})$, representing a generic periodic disturbance originating from a non-axial inflow;
- a constant force $F_{3_{\text{hub}}} = T_{\text{ref}}$ on the hub, along its axis, representing the rotor's aerodynamic thrust; its direction is fixed in the reference system of the hub, and thus follows it when it tilts;
- an internal moment between the hub and the mast, proportional to the opposite of the relative angular velocity, $\mathbf{C}_{\text{hub/mast}} = \mp\gamma(\boldsymbol{\omega}_{\text{hub}} - \boldsymbol{\omega}_{\text{mast}})$, intended to introduce some viscous damping to stabilize the system and limit the amplitude of its oscillations, loosely representing some form of equivalent aerodynamic damping.

[11] The constant c typically has the dimensions of the compliance of a linear or angular spring, depending on the type of constraint.

The values are: $C_{\text{ref}} = 1000$ N·m, $\Omega_{\text{ref}} = 60$ rad/s, $G = 100$ N·m·s/rad, $T_{\text{ref}} = 10000$ N, and $\gamma = 10$ N·m·s/rad. Three models are considered: a reference one, without friction, and two with friction, either the LuGre or the Coulomb model. Three values of the torque disturbance are selected as well, namely $C_d = 100$ N·m, $C_d = 40$ N·m and $C_d = 10$ N·m. The spherical joint radius is $R = 0.04$ m. The LuGre friction model parameters are $\tilde{f}(v_{\text{rel}}) = 0.07$, $\sigma_0 = 2 \cdot 10^6$ m^{-1}, $\sigma_1 = 0$ s $\cdot$ m^{-1}, $\sigma_2 = 0$ s $\cdot$ m^{-1} and $k = 0.71$; the same $\tilde{f}(v_{\text{rel}})$ is used for the Coulomb friction. For each rotor revolution 256 steps are used, which yields a time step of $4.0906 \cdot 10^{-5}$ s.

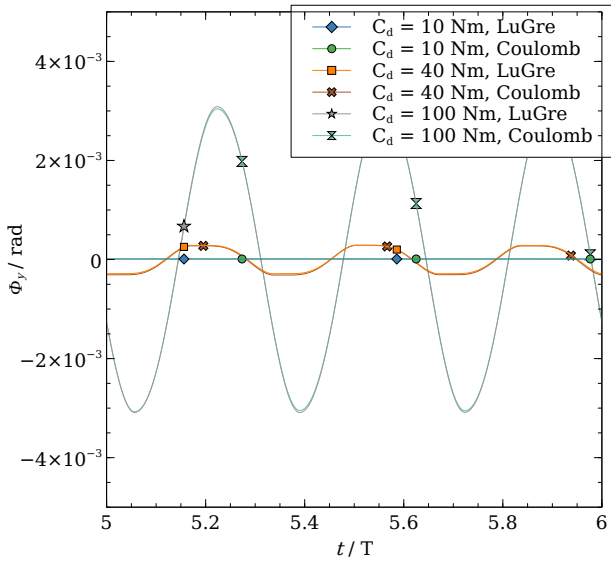

Fig. 11: Gimbal joint: relative rotation Φ_y around joint local axis 2 (time non-dimensionalized with respect to rotor revolution period, T).

The results, obtained for the three disturbance levels, are reported in Figs. 11, where the joint relative rotation Φ_y around the joint local axis 2 is plotted as a function of the mast period. When the disturbance is high enough, as is the case for the results with $C_d = 100$ N·m of Fig. 11, the joint is always sliding, and the friction does not significantly change the system dynamics. With intermediate values of the disturbance, $C_d = 40$ N·m, accounting for friction significantly reduces the joint oscillation perturbation, and the system exhibits stick-slip dynamics, see also Fig. 12, with the rotation angle Φ_y at which stick occurs basically equal for the two friction models. Finally, with the lowest perturbation level of $C_d = 10$ N·m the joint is completely locked when friction is accounted for (Fig. 11), as expected. In all the simulations the results obtained with the LuGre and Coulomb models are very similar, although not identical.

For this specific problem, the Coulomb model requires between 63% and 77% more iterations (Table 4), and up to 50% more computational time, for 2 s of simulation,

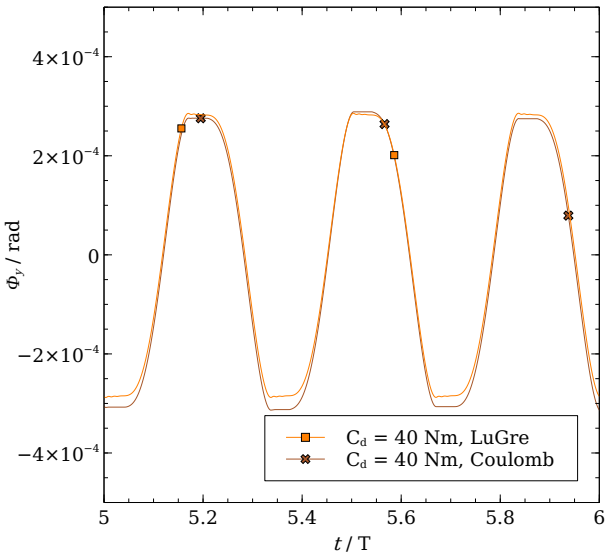

Fig. 12: Gimbal joint: relative rotation Φ_y around joint local axis 2, $C_d = 40$ N·m (time non-dimensionalized with respect to rotor revolution period, T).

Table 4: Gimbal: iterations for 2 s of simulated time, 48894 time steps.

C_d, N·m	**LuGre**	**LuGre/step**	**Coulomb**	**Coulomb/step**	**Coulomb/LuGre** − 1
10	49031	1.0028	79882	1.6338	+63%
40	49560	1.0136	87646	1.7926	+77%
100	49957	1.0217	86848	1.7763	+74%

corresponding to about 19 rotor revolutions and short of 50000 time steps. In practice, the LuGre model always converges in little more than one iteration per time step, whereas the Coulomb one requires between 1.63 and 1.8 iterations per time step, the larger figure occurring in the case dominated by stick-slip transitions, i.e., for $C_d = 40$ N·m.

6 Conclusions

A formulation for the inclusion of friction in revolute and spherical joints within a general-purpose multibody framework has been presented. The formulation represents the normal contact reaction as a primary unknown and expresses friction forces and moments through additional unknowns. The proposed approach extends both Coulomb-type and LuGre-inspired friction models to three-dimensional rotational motion and embeds them consistently within the constrained equations governing multibody dynamics.

Numerical examples demonstrate that the formulation remains robust in the presence of sticking conditions, redundant constraints, and multiple interacting frictional joints. The comparison between the Coulomb and LuGre formulations did not highlight significant differences in the response, at least for the test cases considered here. It is worth noting, however, that the numerical properties and treatment of the two models are significantly different, with the Coulomb model defining an algebraic constraint while sticking, whereas the LuGre model introduces a very stiff internal dynamic. The LuGre model may therefore be relevant when the dynamics of the pre-slip regime need to be represented, for example, in applications involving high-precision position control.

The application to a representative tiltrotor gimbal assembly demonstrated that the proposed methodology can be applied to a system characterized by multiple interacting revolute and spherical joints, redundant constraints, and different friction sources. The use of constraint regularization eliminated constraint redundancy while enabling the preservation of realistic load-transfer mechanisms and maintaining numerical robustness.

The present work represents an initial step toward the systematic inclusion of physically meaningful joint friction models in rotorcraft and aerospace multibody simulations. The results suggest that friction effects, often neglected or excessively simplified, can influence the dynamics and stability of articulated systems in the examples considered.

Future developments will address the identification and calibration of friction parameters from experimental data, the extension to more detailed contact descriptions, and the systematic assessment of friction effects in aeroelastic and aeroservoelastic applications involving complex articulated mechanisms.

Competing Interests

The second author, Pierangelo Masarati, is an Associate Editor of Multibody System Dynamics, but was not involved in the peer review process at any stage. All other authors have no competing interests to declare that are relevant to the content of this article.

Appendix A Spherical Joint Local Coordinate System Initialization

Assuming that $\mathbf{n}$ is the previously defined unit vector aligned with the normal transmitted force $\mathbf{r}_n$, the tangent unit vectors $\mathbf{t}_1$ and $\mathbf{t}_2$ are conveniently constructed as follows:

- $\mathbf{t}_1$: construct a robust unit vector structurally orthogonal to $\mathbf{n}$, namely
  i) find the component of $\mathbf{n}$ of largest modulus, $\mathbf{n}(i_{\max})$:

$$|\mathbf{n}(i_{\max})| = \max_{i=1,2,3} |\mathbf{n}(i)|; \tag{A1}$$

ii) find the component of $\mathbf{n}$ of second largest modulus, $\mathbf{n}(i_{\max -1})$:

$$|\mathbf{n}(i_{\max -1})| = \max_{i=1,2,3\setminus i_{\max}} |\mathbf{n}(i)|\,; \tag{A2}$$

iii) construct a vector $\mathbf{w}$ such that

$$\mathbf{w}(i_{\max}) = \mathbf{n}(i_{\max -1}) \tag{A3a}$$
$$\mathbf{w}(i_{\max -1}) = -\mathbf{n}(i_{\max}), \tag{A3b}$$

and the remaining component equal to zero; by construction, vector $\mathbf{w}$ is orthogonal to $\mathbf{n}$;

iv) set $\mathbf{t}_1$ equal to $\mathbf{w}$ after normalizing it to unit value,

$$\mathbf{t}_1 = \frac{\mathbf{w}}{\|\mathbf{w}\|}. \tag{A4}$$

The norm of $\mathbf{w}$, $\|\mathbf{w}\|$, is surely nonzero by construction because two of its elements correspond to the two largest modulus elements of $\mathbf{n}$, which has unit norm; as such, at least one of them is nonzero and with a value between $1/\sqrt{3}$ and 1.

- $\mathbf{t}_2$: construct a unit vector that is structurally orthogonal to both previous unit vectors, namely
  - compute the vector product between $\mathbf{n}$ and $\mathbf{t}_1$, namely

$$\mathbf{t}_2 = \mathbf{n} \times \mathbf{t}_1. \tag{A5}$$

The resulting vector does not require normalization, since by construction $\mathbf{n}$ and $\mathbf{t}_1$ are orthogonal unit vectors.

The algorithm is uniquely defined and deterministic (the only arbitrariness may occur when sorting the elements of $\mathbf{n}$ if two or more have identical norm). Vectors $\mathbf{n}$, $\mathbf{t}_1$, and $\mathbf{t}_2$ can be used to form the basis for a local reference system tangent to the point of contact, and thus can be used within the spherical joint formulation of Section 4.

References

[1] Armstrong-Hélouvry, B.: Control of Machines with Friction. Kluwer Academic Publishers, New York, NY, USA (1991)

[2] Hachkowski, M.R., Peterson, L.D., Lake, M.S.: Friction model of a revolute joint for a precision deployable spacecraft structure. Journal of Spacecraft and Rockets **36**(4), 591–598 (1999). https://doi.org/10.2514/3.27205

[3] Marques, F., Flores, P., Pimenta Claro, J.C., Lankarani, H.M.: A survey and comparison of several friction force models for dynamic analysis of

multibody mechanical systems. Nonlinear Dynamics **86**(3), 1407–1443 (2016). https://doi.org/10.1007/s11071-016-2999-3

[4] Marques, F., Flores, P., Claro, J.C.P., Lankarani, H.M.: Modeling and analysis of friction including rolling effects in multibody dynamics: a review. Multibody System Dynamics **45**(2), 223–244 (2019). https://doi.org/10.1007/s11044-018-09640-6

[5] Pagani, R., Legnani, G., Incerti, G., Gheza, M.: Evaluation and modeling of the friction in robotic joints considering thermal effects. Journal of Mechanisms and Robotics **12**(2), 021108 (2020). https://doi.org/10.1115/1.4045939

[6] Rathee, R.: Numerical modeling and simulation of friction models for mechanical systems: A brief review. Materials Today: Proceedings (2023). https://doi.org/10.1016/j.matpr.2022.12.185

[7] Sun, G., Ding, Y., Han, S.: Identification of friction in joints for multibody dynamics: a Neural-DAE based approach. Nonlinear Dynamics **113**(20), 27459–27482 (2025). https://doi.org/10.1007/s11071-025-11514-4

[8] Bauchau, O.A., Ju, C.: Modeling friction phenomena in flexible multibody dynamics. Computer Methods in Applied Mechanics and Engineering **195**(50), 6909–6924 (2006). https://doi.org/10.1016/j.cma.2005.08.013

[9] Piedbœuf, J.-C., Carufel, J., Hurteau, R.: Friction and stick-slip in robots: Simulation and experimentation. Multibody System Dynamics **4**(4), 341–354 (2000). https://doi.org/10.1023/A:1009888213333

[10] Lv, Q., He, W., Lu, Z.: Physical models of sliding friction: A review. Friction **14**(4), 9441132 (2026). https://doi.org/10.26599/FRICT.2025.9441132

[11] Fu, Z., Niu, J., Liu, M., Liu, G., Gao, X.: Dynamics modeling of flexible-joint robotic manipulators: a bibliometric review of physics and AI approaches. Nonlinear Dynamics **114**(9), 687 (2026). https://doi.org/10.1007/s11071-026-12571-z

[12] Flores, P.: Contact mechanics for dynamical systems: a comprehensive review. Multibody System Dynamics **54**(2), 127–177 (2022). https://doi.org/10.1007/s11044-021-09803-y

[13] Flores, P., Ambrósio, J., Claro, J.C.P., Lankarani, H.M.: Dynamics of multibody systems with spherical clearance joints. Journal of Computational and Nonlinear Dynamics **1**(3), 240–247 (2006). https://doi.org/10.1115/1.2198877

[14] Canudas de Wit, C., Olsson, H., Åström, K.J., Lischinsky, P.: A new model for control of systems with friction. IEEE Transactions on Automatic Control **40**(3), 419–425 (1995). https://doi.org/10.1109/9.376053

[15] Pennestrì, E., Rossi, V., Salvini, P., Valentini, P.P.: Review and comparison of dry friction force models. Nonlinear Dynamics **83**(4), 1785–1801 (2016). https://doi.org/10.1007/s11071-015-2485-3

[16] Marques, F., Woliński, Ł., Wojtyra, M., Flores, P., Lankarani, H.M.: An investigation of a novel LuGre-based friction force model. Mechanism and Machine Theory **166**, 104493 (2021). https://doi.org/10.1016/j.mechmachtheory.2021.104493

[17] Morandini, M., Masarati, P.: Friction modeling in spherical joints for constrained multibody systems. In: 8th International Conference on Multibody System Dynamics, IMSD2026, Seville, Spain (2026). https://doi.org/10.21203/rs.3.rs-9928159/v1

[18] Masarati, P., Morandini, M., Mantegazza, P.: An efficient formulation for general-purpose multibody/multiphysics analysis. J. of Computational and Nonlinear Dynamics **9**(4), 041001 (2014). https://doi.org/10.1115/1.4025628

[19] Laulusa, A., Bauchau, O.A.: Review of classical approaches for constraint enforcement in multibody systems. J. of Computational and Nonlinear Dynamics **3**(1) (2008). https://doi.org/10.1115/1.2803257

[20] Bauchau, O.A., Laulusa, A.: Review of contemporary approaches for constraint enforcement in multibody systems. J. of Computational and Nonlinear Dynamics **3**(1) (2008). https://doi.org/10.1115/1.2803258

[21] Faraz, A., Payandeh, S.: Towards approximate models of Coulomb frictional moments in: (i) revolute pin joints and (ii) spherical-socket ball joints. Journal of Engineering Mathematics **40**(3), 283–296 (2001). https://doi.org/10.1023/A:1017545030199

[22] Johnson, K.L.: Contact Mechanics. Cambridge University Press, Cambridge (1985). https://doi.org/10.1017/CBO9781139171731

[23] Acary, V., Brémond, M., Huber, O.: In: Leine, R., Acary, V., Brüls, O. (eds.) On Solving Contact Problems with Coulomb Friction: Formulations and Numerical Comparisons, pp. 375–457. Springer, Cham (2018). https://doi.org/10.1007/978-3-319-75972-2_10

[24] Tasora, A., Anitescu, M.: A matrix-free cone complementarity approach for solving large-scale, nonsmooth, rigid body dynamics. Computer Methods in Applied Mechanics and Engineering **200**(5), 439–453 (2011). https://doi.org/10.1016/j.cma.2010.06.030

[25] Dupont, P., Hayward, V., Armstrong, B., Altpeter, F.: Single state elasto-plastic friction models. IEEE Transactions on Automatic Control **47**(5), 787–792 (2002). https://doi.org/10.1109/TAC.2002.1000274

[26] Smirnov, Y.P.: Some frictional effects in a spherical joint. Soviet Applied Mechanics **17**(10), 911–915 (1981). https://doi.org/10.1007/BF00885569

[27] Sage, R.M.: The mathematical modelling of ball-joints with friction. Ph.d. thesis, University of Leicester (1987). https://www.bibliosearch.polimi.it

[28] Waltersson, G.A., Karayiannidis, Y.: Planar friction modeling with LuGre dynamics and limit surfaces. IEEE Transactions on Robotics **40**, 3166–3180 (2024). https://doi.org/10.1109/TRO.2024.3410455

[29] De Vita, P., Cassoni, G., Morandini, M., Masarati, P., Fonte, F., Favale, M., van 't Hoff, S.: Numerical interpretation of whirl flutter in a tiltrotor wind-tunnel model using mid-fidelity aerodynamics and mechanical friction. CEAS Aeronautical Journal (online April 13, 2026; in press). https://doi.org/10.1007/s13272-026-00966-y

[30] van 't Hoff, S., Fonte, F., De Vita, P., Cassoni, G., Masarati, P., Soal, K.: ATTILA tiltrotor whirl flutter code-to-test correlation. In: Vertical Flight Society 81st Annual Forum, Virginia Beach, VA, USA (2025). https://doi.org/10.4050/F-0081-2025-265